Plasmonics (2023) 18:493–502
https://doi.org/10.1007/s11468-022-01781-x

Surface Plasmon Polaritons Filter with Transmission Optimized Based on the Multimode Interference Coupled Mode Theory

Lehui Wang[1] · Hengli Feng[1] · Jingyu Zhang[1] · Zuoxin Zhang[1] · Dongchao Fang[1] · Jincheng Wang[1] · Chang Liu[1] · Yang Gao[1,2]

Received: 25 September 2022 / Accepted: 26 December 2022 / Published online: 6 January 2023
© The Author(s), under exclusive licence to Springer Science+Business Media, LLC, part of Springer Nature 2023

Abstract
In this paper, a novel surface plasmon polaritons (SPPs) multimode filter based on a metal-insulator-metal (MIM) waveguide is investigated. The resonant cavity of the filter consists of four mutually perpendicular rectangular cavities. There are three sharp resonance peaks at 864nm, 966nm, and 1481nm with 5.5%, 10.3%, and 21.3% transmittance, respectively. In addition, the multimode interference coupled mode theory (MICMT) and the standing wave theory are simultaneously utilized to optimize the transmittance. The number of modes increases by adding particular cavities underneath the main waveguide. Furthermore, the other three structures based on the initial structure are proposed to optimize the transmittance of each mode. The four structures show excellent sensitivity (S) and figure of merit (FOM): its maximum is 1435nm/RIU at 1481nm and 87.3 at 863nm, respectively. Moreover, the outstanding biosensing properties of one of the proposed structures are also studied. The proposed filters may have potential applications in the design of highly integrated optical circuit devices.

Keywords Surface plasmon polaritons · Metal-insulator-metal · Multimode interference coupled mode theory

Introduction

Surface plasmon polaritons (SPPs) are evanescent waves that exist at a metal-dielectric interface. They are generated by the interaction of incident electromagnetic waves with free electrons in the metal, and amplitudes decay exponentially in the vertical direction of the metal-dielectric interface [1, 2]. SPPs play a vital role in many aspects because of breaking through the classic diffraction limit and manipulation on subwavelength scales, such as biomedicine, optical system [3] etc. In optical integrated devices based on SPPs, filters have captured more attention from researchers because of the high importance in high-density plasmonic integrated optical circuits for optical processing. MIM waveguide structure is composed of two metal layers and a dielectric layer sandwiched between them, which effectively confine surface plasmons in the waveguide. Therefore, MIM waveguides are very suitable for making surface plasmon filters. In recent years, MIM waveguide structure devices based on SPPs have been widely studied, such as Mach-Zehnder interferometer [4], switch [5, 6], multiplexer and demultiplexer [7, 8], Bragg reflector [9], plasma filter [10] etc.

Currently, numerous resonators, including disk resonators [11–13] and ring resonators [14, 15] based on MIM waveguides have been proposed. Modulation of a specific mode or multiple modes is implemented in these works. The multimode interference coupled mode theory (MICMT) and degenerate interference coupled mode theory (DICMT) based on the Fano resonance were proposed by Li et al. [16, 17]. The filtering effect is not reinforced despite the independent adjustment of the resonance peak. Rectangular cavities were placed at specific locations by Zheng et al to achieve more modes exploiting the MICMT [18]. The method, however, is theoretically unable to determine the geometric parameters and locations of the added rectangle cavities.

In light of this, a MIM waveguide structure filter with a main waveguide and a resonator composed of four rectangular cavities that are perpendicular to one another is proposed.

✉ Yang Gao
gaoy_hit@163.com

1 School of Electronics Engineering, Heilongjiang University, Xuefu Road, Harbin 150080, Heilongjiang, China

2 Heilongjiang Provincial Key Laboratory of Metamaterials Physics and Device, Heilongjiang University, Xuefu Road, Harbin 150080, Heilongjiang, China

One or more rectangular cavities are then placed on the proposed cavity. According to the standing wave theory and the MICMT, the filtering effect can be optimized or the number of modes can be increased by appropriately altering the parameters of the additional cavities. Moreover, the fitting of the finite-difference time-domain (FDTD) simulation graph and the MICMT is realized. The filter may exert a significant impact on the device design in highly integrated optical circuits.

Structure and Theory

The structure 1 (S1) in Fig. 1 is composed of a main waveguide and a resonant cavity. The width of the waveguide is represented by the parameter $w = 50$ nm in the figure. The distance between the resonant cavity and the main waveguide is set to $d = 35$ nm. The lengths of the rectangular cavities in the vertical and horizontal cavities are defined as $L_1 = 210$ nm and $L_2 = 600$ nm, respectively. The separation of the two vertical rectangular cavities is $L_3 = 180$ nm. The simulation is done using FDTD solutions. The calculation region is subjected to the perfect matching layer absorption boundary conditions. At the same time, the space step and the time step are designed $\Delta x = \Delta y = 5$ nm and $\Delta t = \Delta x/2c$ (c is the velocity of light in a vacuum) in order to ensure the stable and accurate process of the numerical simulation. In addition, the incident light along the positive x-axis is TM polarized wave.

The white part of the diagram indicates air (n=1), whereas the light blue part represents silver. The dielectric constant of the metal silver is characterized by Drude model [19]:

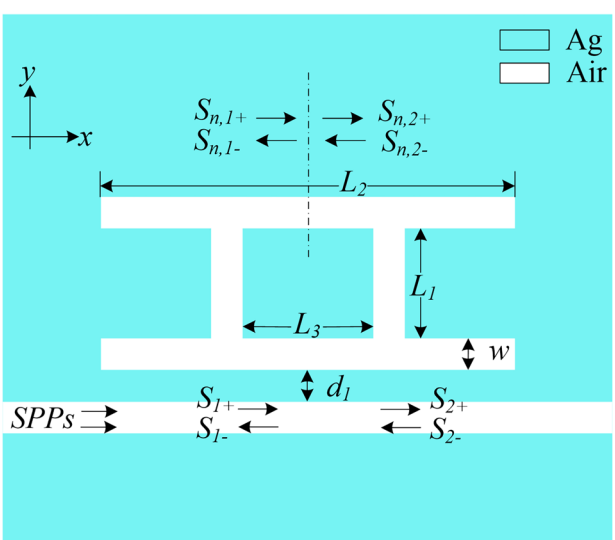

Fig. 1 The schematic diagram of the structure 1

$$\varepsilon_m(\omega) = \varepsilon_\infty - \frac{\omega_p^2}{\omega^2 + i\gamma\omega} \tag{1}$$

where ε_m is the permittivity of the metal, $\varepsilon_\infty = 3.7$ is the relative permittivity at infinite frequency, ω stands for the angular frequency of the incident electromagnetic radiation, $\omega_p = 1.38 \times 10^{16}$rad/s reflects the resonance frequency of the plasma, and $\gamma = 2.73 \times 10^{13}$rad/s represents the damping attenuation frequency at resonance.

Surface plasmons are stimulated after light enters the main waveguide. Then, standing waves are formed when surface plasmon waves are coupled into the cavity. The light wave is confined in the resonant cavity, resulting in the filtering function. In order to create a standing wave in a rectangular cavity, the light must meet the formula below [20]:

$$2k(\omega) \cdot Re(n_{eff})L_{eff} + 2\Delta\varphi = 2m\pi \tag{2}$$

where m is an integer, which represents the number of antinodes of the standing wave. $k(\omega) = 2\pi/\lambda$ is the wave vector in free space, and L_{eff} is the effective length of the electromagnetic wave propagating once in the resonant cavity. The effective length is not a definite parameter but varies with the resonance position [21]. And $\Delta\varphi$ is the phase difference generated by the reflection of SPPs at the end of the rectangular cavity.

Through the above equations, the resonance wavelength can be solved as:

$$\lambda_m = \frac{2L_{eff}Re(n_{eff})}{m} \tag{3}$$

where n_{eff} is the effective refractive index of MIM waveguide structure. According to the dispersion relationship of SPPs, the n_{eff} can be derived that [22]:

$$\frac{\varepsilon_i k_m}{\varepsilon_m k_i} = \frac{1 - e^{k_i w}}{1 + e^{k_i w}} \tag{4}$$

$$k_i = k_0\sqrt{\left(\frac{\beta_{spp}}{k_0}\right)^2 - \varepsilon_i}, \quad k_m = k_0\sqrt{\left(\frac{\beta_{spp}}{k_0}\right)^2 - \varepsilon_m} \tag{5}$$

$$\beta_{spp} = n_{eff}k_0 = n_{eff}\frac{2\pi}{\lambda} \tag{6}$$

where ε_i and ε_m are the permittivities of the insulator and metal, respectively; β_{spp} is the propagation constant of SPPs wave; k_0, k_i, and k_m are the wave vectors in vacuum, insulator and metal, respectively.

In coupled cavity systems, the overall field transmission can be viewed as interference between multiple modes. Therefore, based on the single-mode coupled mode theory,

the MICMT is derived, and the amplitude of any mode can be expressed as follows [16, 23]:

$$\frac{dA_n}{dt} = (i\omega_n - \frac{1}{\tau_{in}} - \frac{1}{\tau_{cn}})A_n + \sqrt{\frac{1}{\tau_{cn}}}S_{n,1+} + \sqrt{\frac{1}{\tau_{cn}}}S_{n,2-} \quad (7)$$

$$S_{2+} = S_{1+} - \sum_n \sqrt{\frac{1}{\tau_{cn}}}A_n \quad (8)$$

$$S_{n,1+} = Ce^{i\varphi_n}S_{1+}, \quad S_{n,2-} = Ce^{i\varphi_n}S_{2-} \quad (9)$$

$S_{i\pm}(i = 1, 2)$ represents the amplitude in each waveguide, where positive sign represents the forward amplitude, and negative sign represents the backward amplitude. $S_{n,i\pm}(i = 1, 2)$ is the forward and backward amplitude for nth order resonant mode. $Ce^{i\varphi_n}$ is the normalization coefficient, where φ_n is total coupled phase difference and $C = 1$. $1/\tau_{cn} = \omega/2Q_c$ and $1/\tau_{in} = \omega/2Q_i$ [24] represent the decay rate of external losses and internal losses, respectively.

The ratio of the normalized amplitude of the output to the normalized amplitude of the input is defined as the transmission coefficient of the SPPs, so the simultaneous Eqs. (7–9) can be derived as:

$$t_n = \frac{S_{2+}}{S_{1+}} = 1 - \sum_n \frac{\frac{1}{\tau_{cn}}Ce^{i\varphi_n}}{i(\omega - \omega_n) + \frac{1}{\tau_{in}} + \frac{1}{\tau_{cn}}} \quad (10)$$

$$T = |t_n|^2 = |1 - \sum_n \frac{\frac{1}{\tau_{cn}}Ce^{i\varphi_n}}{i(\omega - \omega_n) + \frac{1}{\tau_{in}} + \frac{1}{\tau_{cn}}}|^2 \quad (11)$$

The total coupled phase difference φ_n can be approximated as a constant for the convenience of calculation [17].

Simulation Results and Discussions

The transmission spectrum obtained by the FDTD simulations is shown in Fig. 2(a) as a black solid line. It reveals that the structure exhibits three resonance peaks in 800–1600nm, positioned at 864nm (mode 1), 966nm (mode 2), and 1481nm (mode 3), with the corresponding transmittance of 5.6%, 10.7%, and 21.3%, respectively. The transmission response exhibits evidently Lorentz line shape. Furthermore, the simulation results are approximated using MICMT theory, with the amplitude coefficient of each mode being described by Eq. (10), and the overall amplitude value obtained from $t = \sum_{n=1}^{3} t_n$. When the parameter is set to $\tau_{i1} = 244$ fs, $\tau_{i2} = 226.7$ fs, $\tau_{i3} = 248$ fs, $\tau_{c1} = 74.4$ fs, $\tau_{c2} = 108.6$ fs, and $\tau_{c3} = 212.4$ fs, the fitting structure can be obtained as shown

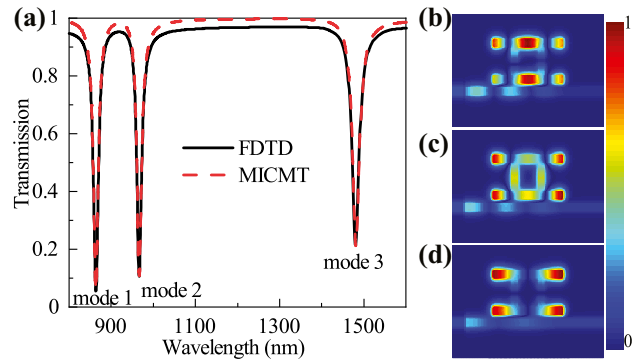

Fig. 2 **a** The transmission spectra (black solid line) for S1 and theoretical fitting based on the MICMT (red dash line). **b–d** Normalized magnetic field distributions at resonance wavelengths of 864nm, 966nm and 1481nm, respectively

by the red dash line in Fig. 2(a). The lines show good fitting between results from FDTD and MICMT theory.

The normalized magnetic field diagrams at the three peaks are displayed in Fig. 2(b)–(d), respectively. The propagation process of SPPs can be clearly seen in the figure. The SPPs propagate into the main waveguide and are coupled to the resonator where is reflected back and forth. If the resonance conditions are met, two light waves in opposite directions with phase differences meet to form a standing wave, thereby confining the light waves in the resonant cavity. Therefore, the resonance peak appears in the transmission spectrum.

Moreover, the influences of the length of the resonator and the distance between the waveguide and the resonator on the transmission spectra are studied. Firstly, variety in L_1 from 190nm to 230nm and L_2 from 580nm to 620nm is researched in Fig. 3(a)–(b), which demonstrate the red-shift phenomenon. The transmittance of other modes is basically steady, and merely that of mode 2 in Fig. 3(a) is slightly increased. The reason for the red-shift is the positive correlation between the length of the rectangular cavity and the effective length. Besides, according to Eq. (3), the increase of the effective length shift red the resonance wavelength. Subsequently, as shown in Fig. 3(c), with L_3 from 140nm to 220nm, mode 1 is red-shift and mode 2 and mode 3 are blue-shift. Finally, the coupling distance d_1 is varied from 30nm to 40nm in 5nm steps, while keeping the other parameters constant. According to the simulation results displayed in Fig. 3(d), d_1 substantially affects the resonance peaks: the transmission spectrum becomes blue-shifted as d_1 increases, and the transmittance at the resonance peaks decreases seriously. This results from the phenomenon that the attenuation rises as the coupling distance increases so as to most of the light is lost from the main waveguide. As demonstrated in Eq. (11), the output transmittance will increase as the delay rate increases. All in all, the transmittance and resonant wavelength can be controlled by modifying the structural parameters.

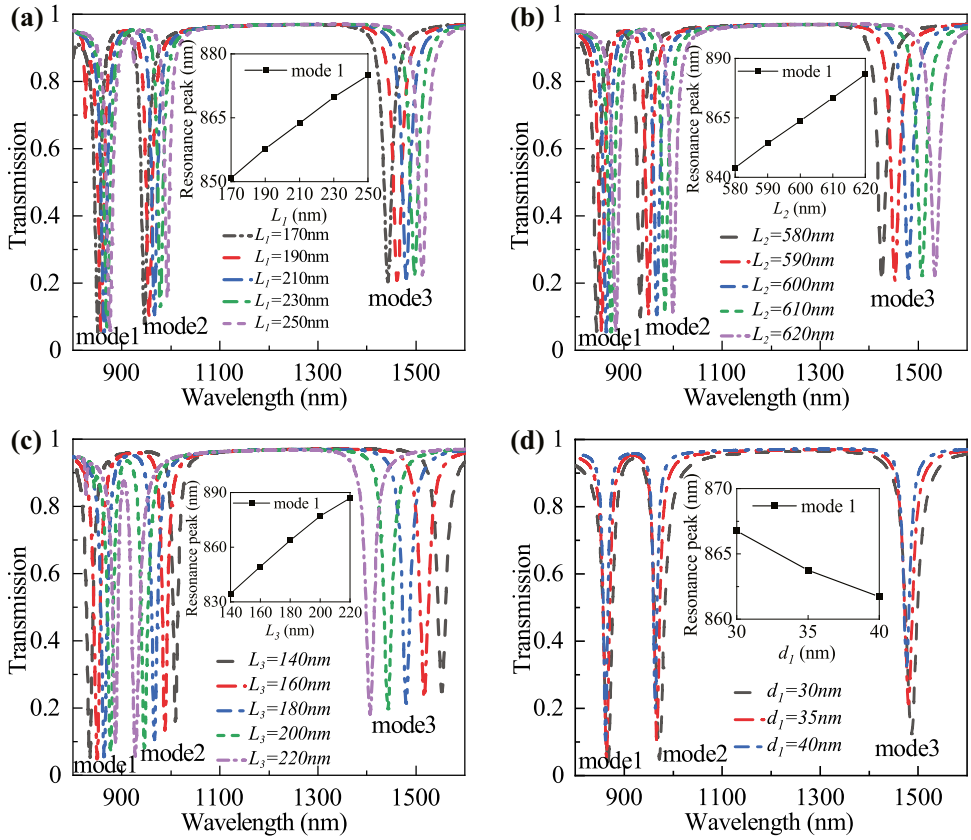

Fig. 3 **a**–**d** Transmission spectra of different L_1, L_2, L_3 and d_1 with constant other parameters and the influence on the resonance peak of mode 1

Variations in transmittance due to fabrication errors inevitably affect the resonance peak of the filter. Accordingly, fabrication tolerance [25] should be considered. In the inserted pictures in Fig. 3, we measure the resonance peak of mode 1 as a function of geometric parameters (L_1, L_2, L_3, d_1). When L_1 and L_3 change in a large range of 80nm, the resonance peaks change by 24nm and 52nm, respectively. It means that the wavelength error induced by L_1 and L_3 errors in fabrication has little impact. And the resonance peak is not sensitive to d_1. Besides, the structure is more sensitive to L_2, and the change of 40nm causes the resonance peak to shift by 39nm. It may be solved by some high-precision fabrication methods, such as focused ion beams (FIB).

The Physical Mechanism of the Mode Increase

Figure 4(a) depicts a new structure (S2) which is added rectangular resonant cavity B with length $L_4 = 500$ nm, width $w = 50$ nm, and separating distance from the main waveguide $d_2 = 40$ nm. The black line in Fig. 4(b) is the simulated transmission spectrum of S2. The number of resonance peaks within 750nm to 1600nm has increased from three to five, which are located at 789nm, 864nm, 966nm, 1479nm and 1541nm, respectively. The corresponding transmittance are 4.08%, 5.54%, 10.31%, 21.43%, and 25.40%, respectively. Comparing Fig. 5(a), (d) and (g), it can be concluded that the resonance wavelength and transmittance of the five

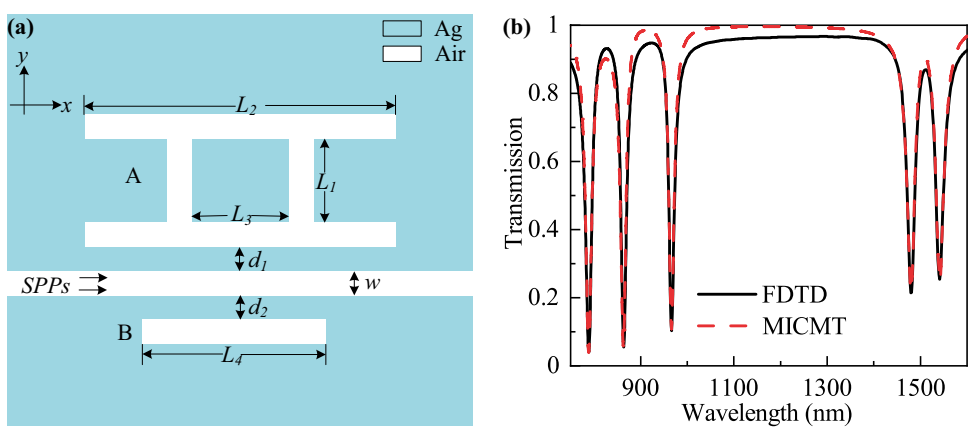

Fig. 4 **a** The schematic diagram of the S2. **b** The transmission spectra (black solid line) for S2 with $L_4 = 500$ nm and theoretical fitting based on the MICMT (red dash line)

modes in Fig. 5(d) correspond to Fig. 5(a) (cavity A) and Fig. 5(g) (cavity B).

Here, the physical mechanism of the mode number increase is investigated in terms of the magnetic field distribution map. There is a simulation in the transmission spectrum and electric field as the two cavities work separately. From Fig. 5(b, e, h) and Fig. 5(c, f, i), when cavity A and cavity B are existence, the mutual interference between them is very weak, so that it can approximately present their respective resonance peak properties. Figure 5(b), (e), and (h) show that most of the energy is not coupled into cavity A but propagates out of the main waveguide. After adding cavity B, however, the energy that is not coupled by cavity A can form a standing wave in cavity B, causing the output to drop sharply. The opposite is true for Fig. 5(c), (f), and (i). Therefore, it is clear from the analysis of the magnetic field that these two sets of peaks are caused by different factors and thus can be adjusted independently.

Furthermore, the phenomenon can be fitted by MICMT in the Eq. (10) with the number of modes $n = 5$, as shown by the red dash line in Fig. 4(b). At this time, the external loss, internal loss and phase difference of each mode are obtained as $\tau_{c1} = 74.4fs$, $\tau_{c2} = 108.6\,\text{fs}$, $\tau_{c3} = 212.4\,\text{fs}$, $\tau_{c4} = 52.9\,\text{fs}$, $\tau_{c5} = 224\,\text{fs}$, $\tau_{i1} = 244\,\text{fs}$, $\tau_{i2} = 226.7\,\text{fs}$, $\tau_{i3} = 248\,\text{fs}$, $\tau_{i4} = 205.6\,\text{fs}$, $\tau_{i5} = 234.6\,\text{fs}, \varphi_1 = 0, \varphi_2 = -0.05\pi, \varphi_3 = 0.05\pi, \varphi_4 = 0.01\pi$, $\varphi_5 = -0.07\pi$. It is consistent with the black solid line, thus proving the correctness of the previous analysis.

Transmission Optimization for One Mode

The filtering effect of S1 is far from the ideal. Therefore, another cavity of specific length is added below the main

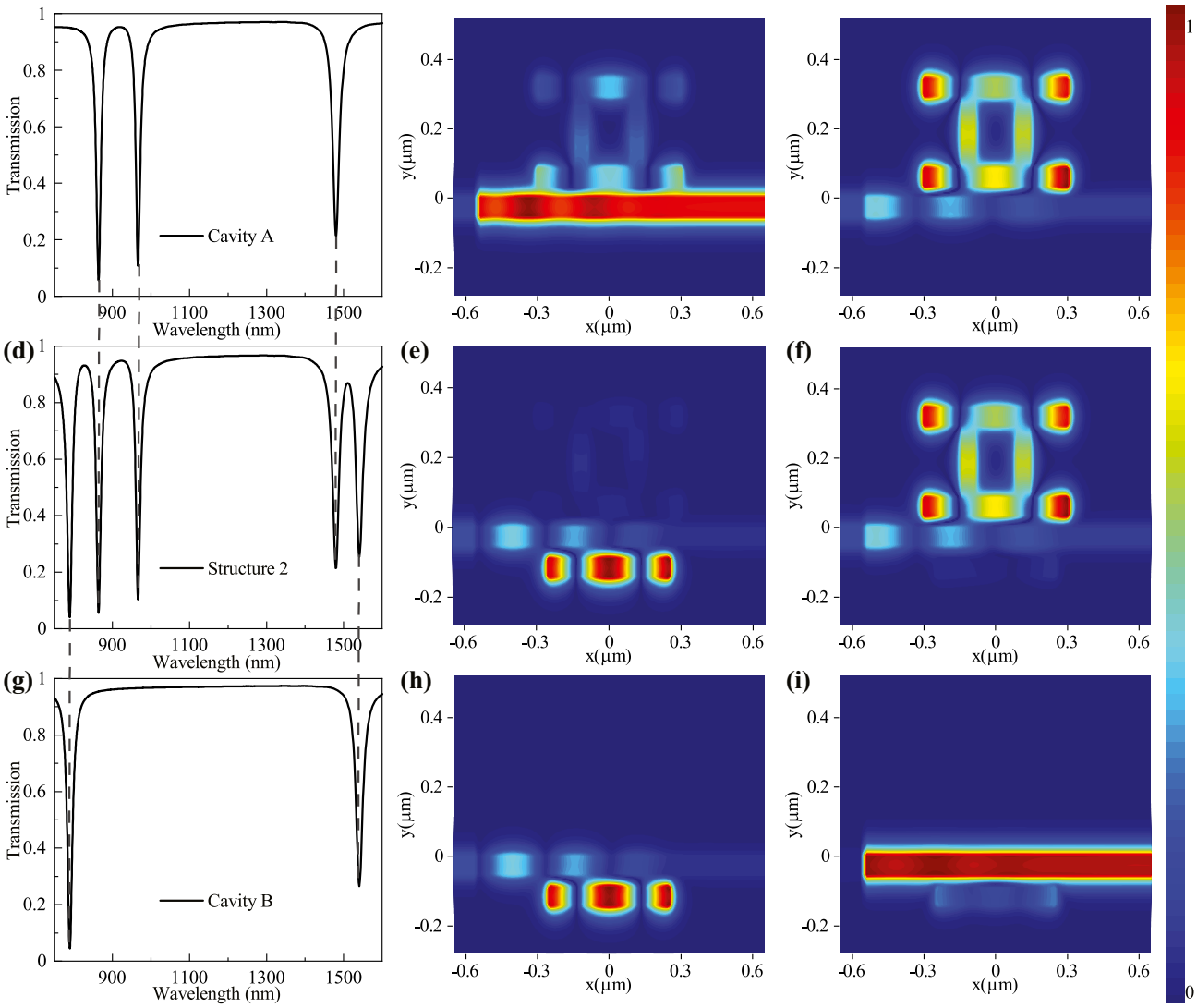

Fig. 5 **a**, **d**, **g** The transmission spectra of S1, S2 and cavity B. **b**, **e**, **h** The normalized magnetic field distribution at 789nm for S1, S2 and cavity B. **c**, **f**, **i** The normalized magnetic field distribution at 966nm for S1, S2 and cavity B

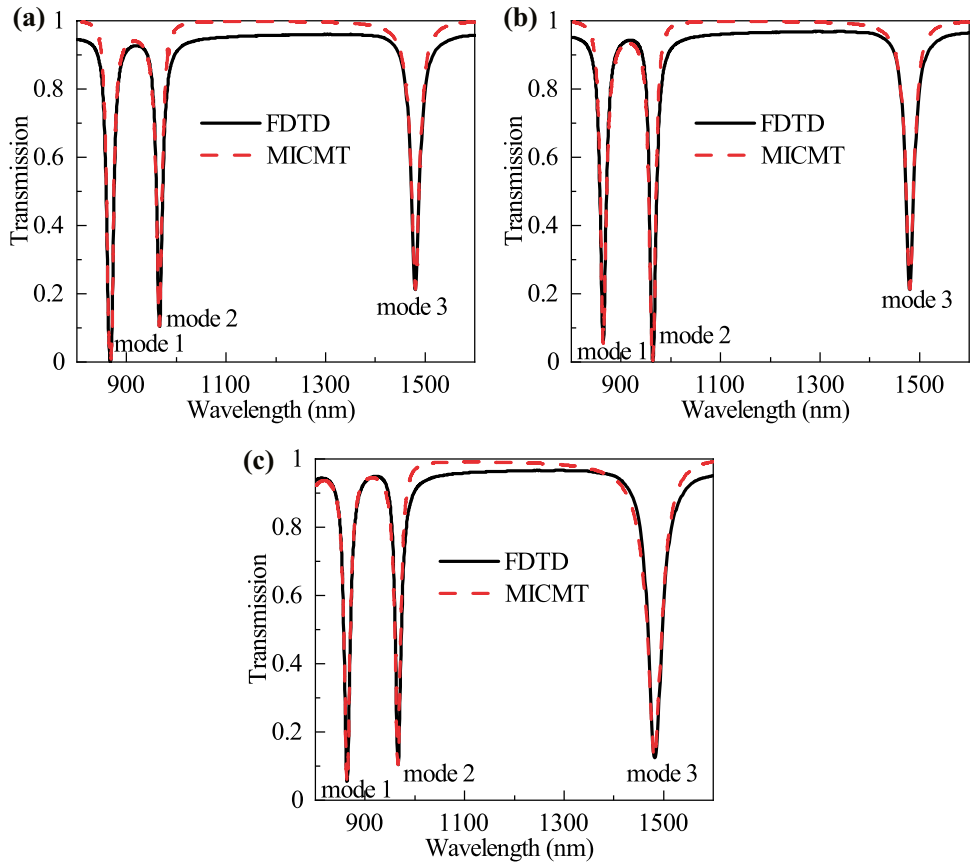

Fig. 6 The transmission spectra (black solid line) for S1 and theoretical fitting based on the MICMT (red dash line) with $L_4 = 264$nm, $L_4 = 295$nm, and $L_4 = 480$nm, respectively

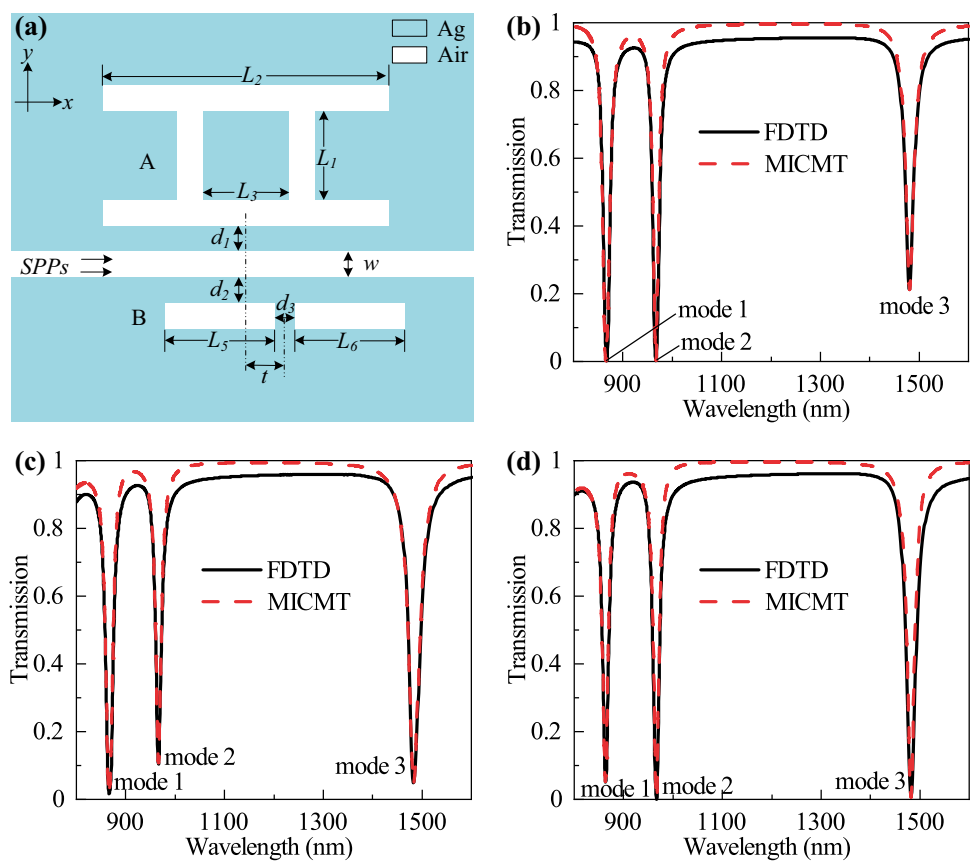

Fig. 7 **a** The schematic diagram of the S3. The transmission spectra (black solid line) for S3 and theoretical fitting based on the MICMT (red dash line) with **b** $L_5 = 264$nm and $L_6 = 295$nm, **c** $L_5 = 295$nm and $L_6 = 480$nm, **d** $L_5 = 264$nm and $L_6 = 480$nm, respectively

Table 1 Transmittance change at the resonant wavelength before (T) and after (T') adding the cavities shown in Fig. 7(b)–(d)

	Fig. 7(b)		Fig. 7(c)		Fig. 7(d)	
	mode 1	mode 2	mode 1	mode 3	mode 2	mode 3
T	5.6%	10.7%	5.6%	21.3%	10.7%	21.3%
T'	0.5%	0.09%	1.6%	4.8%	0%	0.8%

waveguide. According to the analysis in the "Structure and Theory'' section, as long as the wavelength of the incident light satisfies the standing wave conditions of the upper and lower cavities at the same time, the transmittance at the resonance wavelength can be markedly reduced. As shown in Fig. 6(a), when the length of the rectangular cavity is $L_4 = 264$ nm, the transmittance of mode 1 drops sharply from 5.6% to nearly 0.

In fact, given the known resonance wavelength, the theoretical length of L_4 can be calculated by standing wave theory. For mode 1, the effective refractive index is known to be $n_{eff} = 1.436$. According to Eq. (3), the theoretical length of cavity B is 301 nm, while the actual value is 264 nm. This is because standing wave theory only deals with the effective length L_{eff} and effective refractive index n_{eff}, but the waveguide width w and distance d_2 which are ignored also have effects on the resonant wavelength [20].

Then, the other two modes are optimized by changing the length of L_4. When $L_4 = 295$ nm (the standing wave theoretical value is 338nm), the transmittance of mode 2 is optimized, falling from 10.3% to 0.27% at 968nm; when $L_4 = 480$ nm (the standing wave theoretical value is 523nm), mode 3 is optimized, dramatically reducing the transmittance from 21.3% to 12.4% at 1481nm, as illustrated by the black line in Fig. 6(b)–(c). The MICMT is also used to analyze the above results as shown by the red dash line in Fig. 6(a)–(c), and the MICMT results are in agreement with the simulation results.

Transmission Optimization for Two Modes

To enhance both modes at the same time, two rectangular cavities are placed below the main waveguide. This structure is called S3. Despite the fact that a cavity can generate multiple modes, the principle of their resonance is the same. As a result, altering the parameters results in all modes moving simultaneously, making it difficult to enhance two specific modes. Therefore, the simplest solution is to place two cavities underneath, each independently controlling a mode, allowing for dual-mode simultaneous enhancement. At the same time, the distance d_3 between the cavities should be sufficient to avoid the plasma induced transparency effect generated by the coupling between the cavities. Here, it is set to 100 nm.

In S3 of Fig. 7(a), the lengths of the additional resonant cavity are L_5 and L_6, respectively; the distance between the main waveguide and the rectangle cavity is $d_1 = d_2 = 40$ nm. A new parameter, the degree of deviation from the symmetry axis of cavity A is $t = 56$ nm. As shown in Fig. 7(b)–(d), mode 1 and mode 2 are optimized when the length of the additional resonant cavity is $L_5 = 264$ nm, and $L_6 = 295$ nm. Mode 3 and mode 1 are improved with $L_5 = 480$ nm, and $L_6 = 264$ nm. Moreover, mode 2 and mode 3 are enhanced when the parameters are $L_5 = 295$ nm, and $L_6 = 480$ nm. In addition, the simulation results (solid black line) are consistent with the theoretical fit curve of MICMT (dashed red line). Table 1 presents the transmittance changes after adding different resonators.

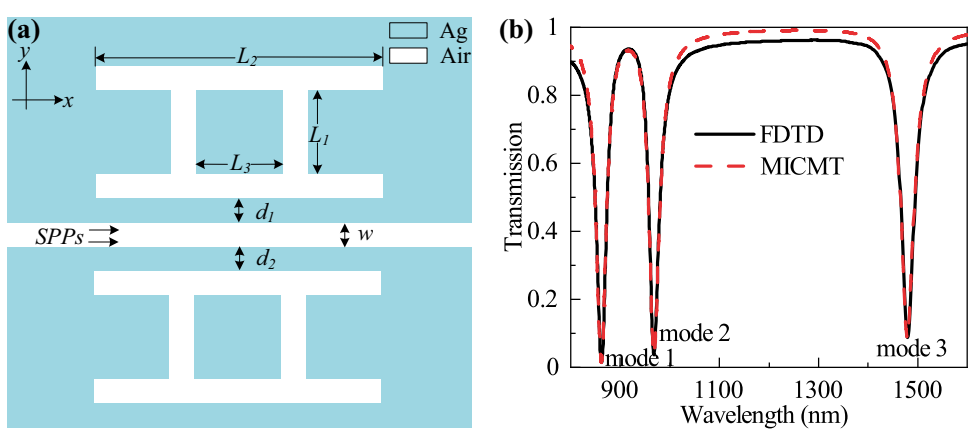

Fig. 8 **a** The schematic diagram of the S4. **b** The transmission spectra (black solid line) for S4 and theoretical fitting based on the MICMT (red dash line)

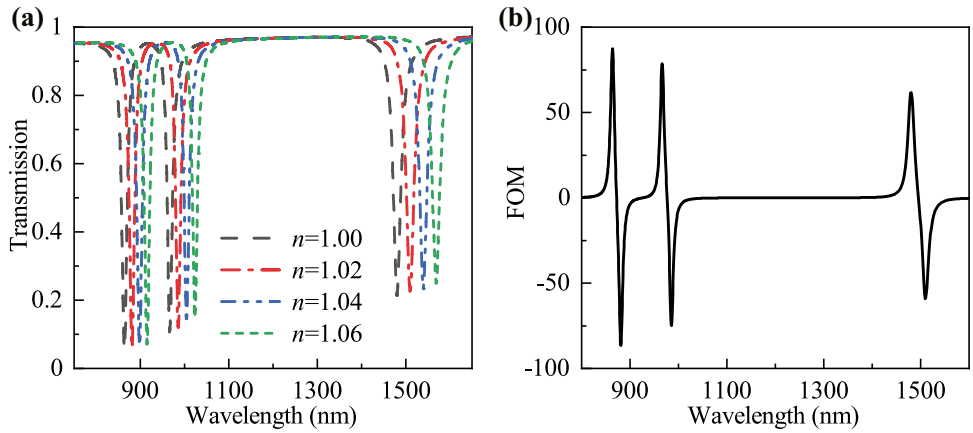

Fig. 9 **a** The transmission spectra of S4 with different refractive indices of the insulator. **b** The FOM curve of the S4

Transmission Optimization for Three Modes

It is inferred from the above analysis that inserting three rectangular cavities beneath the main waveguide can concurrently enhance all three modes of S1. However, the three rectangular cavities arranged side by side dramatically expand the width of Structure 4 (S4). Therefore, symmetry is introduced to enhance all modes of the S1 [11]. S1 is symmetrical around the x-axis to obtain S4 as depicted in Fig. 8(a). The theoretical fitted transmission spectrum of MICMT (red dash line) and the FDTD simulated transmission spectrum (black solid line) are presented in Fig. 8(b). After optimization, the transmittance of mode 1 drops from 5.5% to 1.3%, mode 2 decreases from 10.3% to 4.2%, and mode 3 falls from 21.3% to 8.8%.

Biosensing Properties of Structures

The application of structure in sensing is investigated. Figure 9(a) exhibits that the refractive index of the insulator of S4 transforms in the range of 1 to 1.06, and the transmission spectrum is red-shift. According to the sensitivity formula [26]: $S = \Delta\lambda/\Delta n$, where $\Delta\lambda$ and Δn present the variation in resonance wavelength and refractive index relative to those of air, the sensitivity of S1 at 864 nm is calculated to be 873 nm/RIU, 964 nm/RIU at 966 nm and 1435 nm/RIU at 1481 nm. Then the sensitivities of the four structures are measured as indicated in Table 2.

In addition, the figure of merit (*FOM*) is a crucial factor for evaluating the structure, the quality factor with wavelength can be calculated by [27]:

$$FOM = \frac{2(T_2 - T_1)}{(T_2 + T_1)(n_2 - n_1)} \tag{12}$$

The *FOM* curves are depicted in Fig. 9(b). The *FOM* at the three peaks is 87.31, 78.67, and 61.58, respectively. Subsequently, the *FOM* of the four structures mentioned in this paper is probed and listed in Table 3. What is striking in Tables 2 and 3 is that *S* and *FOM* are optimized.

Finally, the biosensing property of the proposed structure is as well researched. The sensitivity of S4 to four materials (pepsin, plasma, hemoglobin, and glucose) is investigated. The refractive index of the sample can be obtained from the literature [28–30]. Table 4 describes the material name, refractive index (n), the resonance wavelength of mode 3, and the maximum sensitivity (S_{max}) of S4 when filled with different biomaterials. According to the sensitivity formula, the sensitivity of S4 for detecting four biological samples is 1487nm/RIU, 1489nm/RIU, 1482nm/RIU, and 1483nm/RIU. The sensitivity of the filter is high enough for biosensing.

Table 2 The sensitivity of S1, S2 (L_4 = 295 nm), S3 (L_5 = 264 nm, L_6 = 295 nm), and S4

Structure	mode 1	mode 2	mode 3
S1	847	914	1433
S2	841	938	1433
S3	853	932	1433
S4	873	964	1435

Table 3 The *FOM* of S1, S2 (L_4 = 295 nm), S3 (L_5 = 264 nm, L_6 = 295 nm), and S4

Structure	mode 1	mode 2	mode 3
S1	87.21	78.5	61.56
S2	86.78	99.64	60.78
S3	98.69	99.98	61.2
S4	95.66	90.9	79.94

Table 4 The material name, refractive index (n), the resonance wavelength of mode 3, and maximum sensitivity (S_{max}) of S4

Material	n	mode 3 (nm)	S_{max}(nm/RIU)
Pepsin	1.335	1977	1487
Blood plasma	1.35	2000	1489
Hemoglobin	1.38	2042	1482
Glucose	1.4	2072	1483

Conclusion

A unique three-channel filter made up of four mutually perpendicular rectangular cavities and the main waveguide is presented in this paper. Investigation results display that filtering can be optimized and the number of modes can be increased by adding a particular structure below the main waveguide. This phenomenon can be calculated by the multimode interference coupling theory and standing wave theory, and the theoretical results fit well with the FDTD solutions. Furthermore, the sensitivities and FOM of the four structures are measured and the biosensing properties of the S4 are analyzed. This structure which can achieve transmission optimization and mode enhancement effects can be fully utilized in highly integrated optical circuits.

Author Contributions All authors contributed to the study's conception and design. Methodology, material preparation, and data collection were performed by Lehui Wang, Hengli Feng, Jingyu Zhang, and Zuoxin Zhang. Analysis, data curation, and graph drawing were carried out by Dongchao Fang, Jincheng Wang, and Chang Liu. The first draft of the manuscript was written by Lehui Wang, and Yang Gao commented on a previous version of the manuscript. All authors read and approved the final manuscript.

Funding This work was supported by Natural Science Foundation of Heilongjiang Province (LH2019F047), Heilongjiang University Youth Science Fund Project (QL201301), Heilongjiang University Outstanding Youth Science Fund (JCL201404), The Science and Technology Research Project of the Education Department of Heilongjiang Province (12541633), and The Graduate Innovation and Scientific Research Program of Heilongjiang University (YJSCX2022-076HLJU).

Data Availability The simulation come from FDTD simulation results and programming calculations for the theoretical formulas.

Materials Availability The material properties come from the FDTD material library.

Code Availability All codes included in this paper are available upon request by contact with the corresponding author.

Declarations

Ethics Approval Not applicable. This manuscript does not contain experiments on ethical issue.

Consent to Participate Not applicable

Consent for Publication Not applicable

Competing Interests The authors declare no competing interests.

References

1. Barnes WL, Dereux A, Ebbesen TW (2003) Surface plasmon subwavelength optics. Nature 424(6950):824–830. https://doi.org/10.1038/nature01937
2. Bozhevolnyi SI, Volkov VS, Devaux E et al (2006) Channel plasmon subwavelength waveguide components including interferometers and ring resonators. Nature 440(7083):508–511. https://doi.org/10.1038/nature04594
3. Liu L, Han Z, He S (2005) Novel surface plasmon waveguide for high integration. Opt Express 13(17):6645–6650. https://doi.org/10.1364/OPEX.13.006645
4. Singh L, Zhu G, Kumar GM et al (2021) Numerical simulation of all-optical logic functions at micrometer scale by using plasmonic metal-insulator-metal (mim) waveguides. Opt Laser Technol 135(106):697. https://doi.org/10.1016/j.optlastec.2020.106697
5. Karimi Y, Kaatuzian H, Tooghi A et al (2021) All-optical plasmonic switches based on fano resonance in an x-shaped resonator coupled to parallel stubs for telecommunication applications. Optik 243(167):424. https://doi.org/10.1016/j.ijleo.2021.167424
6. Nurmohammadi T, Abbasian K, Yadipour R (2018) Ultra-fast all-optical plasmonic switching in near infra-red spectrum using a kerr nonlinear ring resonator. Optics Communications 410:142–147. https://doi.org/10.1016/j.optcom.2017.09.082
7. Aparna U, Kumar MS (2022) Ultra-compact plasmonic unidirectional wavelength multiplexer/demultiplexer based on slot cavities. Opt Rev 1–8. http://doi.org/10.1007/s10043-022-00722-7
8. Udupi A, Madhava SK (2021) Plasmonic coupler and multiplexer/demultiplexer based on nano-groove-arrays. Plasmonics 16(5):1685–1692. https://doi.org/10.1007/s11468-021-01430-9
9. Zeng L, Li J, Cao C et al (2022) An integrated-plasmonic chip of bragg reflection and mach-zehnder interference based on metal-insulator-metal waveguide. Photonic Sensors 12(3):1–10. https://doi.org/10.1007/s13320-022-0650-0
10. Khani S, Danaie M, Rezaei P (2019) Size reduction of mim surface plasmon based optical bandpass filters by the introduction of arrays of silver nano-rods. Phys E 113:25–34. https://doi.org/10.1016/j.physe.2019.04.015
11. Shi S, Wei Z, Lu Z et al (2015) Enhanced plasmonic band-pass filter with symmetric dual side-coupled nanodisk resonators. J Appl Phys 118(14):143103. http://doi.org/10.1063/1.4932668
12. Lu H, Liu X, Mao D et al (2010) Tunable band-pass plasmonic waveguide filters with nanodisk resonators. Opt Express 18(17):17922–17927. https://doi.org/10.1364/OE.18.017922
13. Qi Y, Zhou P, Zhang T et al (2019) Theoretical study of a multichannel plasmonic waveguide notch filter with double-sided nanodisk and two slot cavities. Results in Physics 14(102):506. https://doi.org/10.1016/j.rinp.2019.102506
14. Pang S, Zhang Y, Huo Y et al (2015) The filter characteristic research of metal-insulator-metal waveguide with double overlapping annular rings. Plasmonics 10(6):1723–1728. https://doi.org/10.1007/s11468-015-9990-6
15. Dong L, Xu X, Sun K et al (2018) Sensing analysis based on fano resonance in arch bridge structure. J Phys Commun 2(10):105010. https://doi.org/10.1088/2399-6528/aae22e
16. Li S, Zhang Y, Song X et al (2016) Tunable triple fano resonances based on multimode interference in coupled plasmonic resonator

system. Opt Express 24(14):15351–15361. https://doi.org/10.1364/OE.24.015351
17. Li S, Wang Y, Jiao R et al (2017) Fano resonances based on multimode and degenerate mode interference in plasmonic resonator system. Opt Express 25(4):3525–3533. https://doi.org/10.1364/OE.25.003525
18. Li Z, Wen K, Chen L et al (2019) Control of multiple fano resonances based on a subwavelength mim coupled cavities system. IEEE Access 7:59369–59375. https://doi.org/10.1109/ACCESS.2019.2914466
19. Palizvan P, Olyaee S, Seifouri M (2018) An optical mim pressure sensor based on a double square ring resonator. Photonic Sensors 8(3):242–247. https://doi.org/10.1007/s13320-018-0491-z
20. Zhang Q, Huang XG, Lin XS et al (2009) A subwavelength coupler-type mim optical filter. Opt Express 17(9):7549–7554. https://doi.org/10.1364/OE.17.007549
21. Wang S, Li Y, Xu Q et al (2016) A mim filter based on a side-coupled crossbeam square-ring resonator. Plasmonics 11(5):1291–1296. https://doi.org/10.1007/s11468-015-0174-1
22. Han Z, Forsberg E, He S (2007) Surface plasmon bragg gratings formed in metal-insulator-metal waveguides. IEEE Photonics Technol Lett 19(2):91–93. https://doi.org/10.1109/LPT.2006.889036
23. Wang Y, Xie YY, Ye YC, Du YX, Liu BC, Zheng WJ, Liu Y (2018) Exploring a novel approach to manipulating plasmon-induced transparency. Opt Commun 427:505–510 S0030401818306102. https://doi.org/10.1016/j.optcom.2018.07.018
24. Li Q, Wang T, Su Y et al (2010) Coupled mode theory analysis of mode-splitting in coupled cavity system. Opt Express 18(8):8367–8382. https://doi.org/10.1364/OE.18.008367
25. Du Y, Shi L, Hong M et al (2013) A surface plasmon resonance biosensor based on gold nanoparticle array. Optics Communications 298:232–236. https://doi.org/10.1016/j.optcom.2013.02.024
26. Yu Z, Fan S (2011) Extraordinarily high spectral sensitivity in refractive index sensors using multiple optical modes. Opt Express 19(11):10029–10040. https://doi.org/10.1364/OE.19.010029
27. Yu S, Zhao T, Yu J et al (2019) Tuning multiple fano resonances for on-chip sensors in a plasmonic system. Sensors 19(7). http://doi.org/10.3390/s19071559
28. Al Mahmod MJ, Hyder R, Islam MZ (2018) A highly sensitive metal-insulator-metal ring resonator-based nanophotonic structure for biosensing applications. IEEE Sens J 18(16):6563–6568. https://doi.org/10.1109/JSEN.2018.2849825
29. Cole T, Kathman A, Koszelak S et al (1995) Determination of local refractive index for protein and virus crystals in solution by mach-zehnder interferometry. Anal Biochem 231(1):92–98. https://doi.org/10.1006/abio.1995.1507
30. Rakhshani MR (2021) Refractive index sensor based on dual side-coupled rectangular resonators and nanorods array for medical applications. Opt Quant Electron 53(5):1–14. https://doi.org/10.1007/s11082-021-02857-4

Publisher's Note Springer Nature remains neutral with regard to jurisdictional claims in published maps and institutional affiliations.

Springer Nature or its licensor (e.g. a society or other partner) holds exclusive rights to this article under a publishing agreement with the author(s) or other rightsholder(s); author self-archiving of the accepted manuscript version of this article is solely governed by the terms of such publishing agreement and applicable law.